JCTC Journal of Chemical Theory and Computation

Dynamics of the Staudinger Reaction

Wei Quan Tian† and Yan Alexander Wang*

Department of Chemistry, University of British Columbia, Vancouver, British Columbia V6T 1Z1, Canada

Received October 14, 2004

Abstract: The Staudinger reaction of phosphane and azide has been investigated by Atom-centered Density Matrix Propagation (ADMP) approach to ab initio molecular dynamics (AIMD) in combination with molecular orbital analysis within density functional theory. At room temperature, the reaction pathway with the cis initial attack dominates the Staudinger reaction. Electrostatic interaction, charge transfer, and covalent overlap are responsible for the initial attack and for the system to overcome the initial reaction barrier. The rotation of PH_3 and PH vibrations facilitate the isomerization of the system from cis intermediate to the last transition state, which indicates that small substituent groups on phosphane can facilitate the last stage of the Staudinger reaction. During the course of the reaction, the change of the average polarizability correlates positively to the change of the potential energy of the system, which clearly suggests that polar solvents can facilitate the overall reaction by stabilizing all transition states and reducing all reaction barriers.

I. Introduction

Staudinger reactions are widely utilized in organic chemistry[1−4] and biology.[5] In a Staudinger reaction, phosphane (**A**) reacts with azide (**B**) to produce phosphazene (**C**) and nitrogen gas[1] (as shown in Scheme 1). With density functional theory (DFT), we investigated reaction mechanisms of Staudinger reactions and identified four initial reaction pathways.[6] The cis-reaction pathway is the most accessible for Staudinger reactions.[6−8] Both of the cis- and trans-intermediates were observed in experiments;[9−11] the existence of the trans-intermediate is the result of isomerization from the cis-intermediate.[6,8] The initial trans-reaction barrier is much higher than the initial cis-reaction barrier.[6,8] The remaining two initial reaction pathways, gamma and concerted attacks (as shown in Scheme 1), were also studied.[6] The concerted initial reaction can be realized with appropriate substituent groups on phosphane and azide. The one-step gamma initial reaction has a reaction barrier lower than the trans-initial reaction barrier but higher than the cis-initial reaction barrier. The trans-initial reaction is always unfavorable because there is only electrostatic attraction between P and N_α to stabilize the transition state, while P can have electrostatic attractions with both N_α and N_γ in the cis- and concerted transition states.[6] From a long distance (e.g. 4 Å), P in phosphane has electrostatic attractions with N_α and N_γ and electrostatic repulsion with N_β in both the initial cis- and concerted transition states. The electrostatic attraction is much stronger than the electrostatic repulsion as indicated by the natural charges of these atoms (as shown in Scheme 1). In the initial concerted transition state, the large distortion of N_3 backbone in azide from nearly linear structure is an unfavorable factor compared with the more open initial cis-transition state. However, the preference of the cis-initial attack has not been fully understood dynamically. Even with conventional quantum mechanical (QM) calculations on the stationary points of the potential energy surface (PES), the dynamical information of preference of the initial reaction pathway is not clear, especially about the interaction of phosphane with azide during the initial reaction phase.

After the initial reaction, two possible cis-intermediates (**cis** or **cisclose** as illustrated in Scheme 2) form. Among these two cis-intermediates, only the **cis** can isomerize to a trans-intermediate (**trans**).[6] Both cis-intermediates can proceed forward to form another intermediate (**int**) and to reach the

* Corresponding author e-mail: yawang@chem.ubc.ca.
† Current address: Department of Molecular and Material Science, Interdisciplinary Graduate School of Engineering Sciences, Kyushu University, 6-1 Kasugakoen, Kasuga, Fukuoka 816-8580, Japan.

10.1021/ct049918x CCC: $30.25
Published on Web 04/19/2005

Scheme 1. Illustration of the Staudinger Reaction of Phosphane (PR_3) + Azide (N_3R')[a]

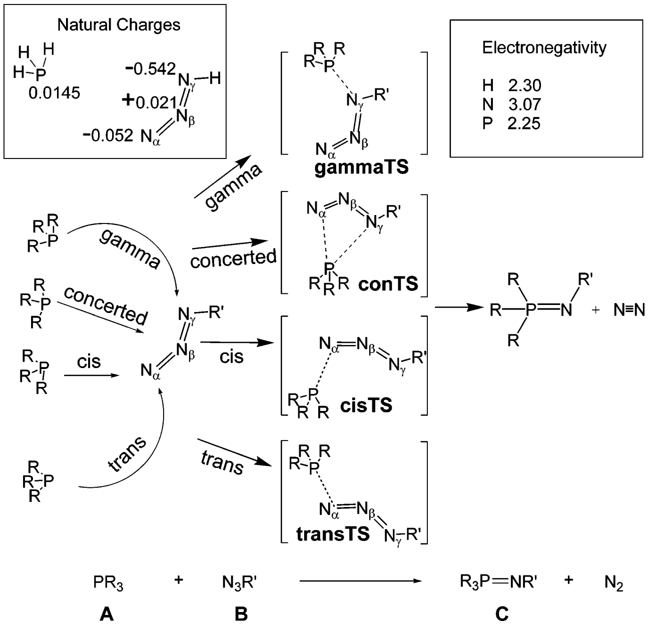

[a] The electronegativities are from ref 12; the charges are from nature charge analysis.

Scheme 2. Possible Reaction Pathways for the Staudinger Reaction[a]

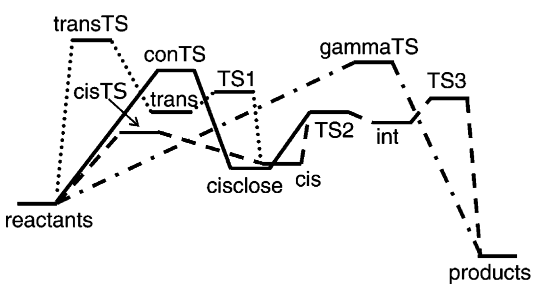

[a] Adapted from ref 6.

final products (phosphazene and N_2).[6] Our studies[6] and other theoretical works[7,8] indicated that the PES is very flat at the N_2 dissociation region around **TS3** (as shown in Scheme 2). Intrinsic reaction coordinate[13] model can locate the minimum energy reaction pathway starting from a transition state; however, the dynamic detail of a reaction pathway starting from a minimum could not be explored with this model.

Molecular dynamics (MD) involving propagation of nuclei in molecule on the PES by solving Newton's equation of motion provides rich information about reactivity and dynamics of a system. The PES could be obtained by fitting to experimental or computational data. However, for polyatomic systems, the experimental data for dynamics are sparse and PES fitting is not a trivial task. Empirical force field has gained wide popularity especially in MD simulations of large systems (e.g. in biology,[14,15] solid-state physics and surface science[16]). Nonetheless, when the quantum effect is important, classical trajectory simulation with the empirical force field cannot produce qualitatively correct result. QM force field, also known as ab initio MD (AIMD) or quantum mechanical MD (QMMD), is a natural choice to overcome this difficulty. In AIMD, (classical) nuclei move on the electronic PES whose energy and derivatives are calculated directly from ab initio methods. Born−Oppenheimer MD (BOMD)[17] methods and extended Lagrangian MD (ELMD) methods are two major flavors of AIMD. In BOMD, the electronic structure calculation is fully converged at each nuclear configuration. While in ELMD, both the electronic wave function and the nuclei are treated as dynamical variables and are propagated simultaneously. The time-consuming feature of BOMD refrains its broad applications. ELMD, which produces comparable dynamics of nuclei to that from BOMD but with lower cost, has been embraced in both physics and chemistry communities, especially since the seminal work of Car and Parrinello.[18] Car-Parrinello MD (CPMD) is a prototype of ELMD. Aimed to treat condensed phases, CPMD employs pseudopotentials and a large number of plane-wave basis functions, which are natural choices for describing condensed phases.[19] It is possible to use atom-centered Gaussian basis function to carry out CPMD,[20−22] although a strict energy conservation problem remains to be solved.[20] In molecular systems of chemical reactions in solution or in gas phase, atom-centered basis functions are more chemically intuitive choices due to their localized nature. Recently, atom-centered density matrix propagation (ADMP) based MD emerged[23−26] and paved a new way to perform AIMD simulations. This new method provides a "novel and robust computational tool to perform AIMD",[24] especially for chemical reactions. Kohn−Sham molecular orbitals are propagated in conventional CPMD,[20−22] while it is the single-particle density matrix that is propagated with nuclei in ADMP.[23−26] Of course, other variables can also be propagated in AIMD.[27]

In present work, with ADMP, we will study the details of the initial Staudinger reaction of (PH_3 + N_3H) and subsequent isomerization of the cis-initial intermediate. The details of the reaction mechanisms of this reaction have been reported before.[6−8] In combination with molecular electronic theory, we will shed lights on the detailed molecular orbital interactions of the two reactants in the initial reaction stage.

II. Computational Methods

The initial applications[25] and analysis[26] on ADMP manifested that ADMP produces a similar PES to that of BOMD while possess some advantages over the plane-wave based CPMD, e.g. ADMP has no systematic bias due to the fictitious electronic mass in computing molecular properties.[25] In ADMP with orthonormal basis, an extended Lagrangian for a system is[23]

$$\pounds = \frac{1}{2}\mathrm{Tr}(\mathrm{V}^{\mathrm{T}}\mathrm{MV}) + \frac{1}{2}\mu\mathrm{Tr}(\mathrm{WW}) - \mathrm{E}(\mathrm{R,P}) - \mathrm{Tr}[\Lambda(\mathrm{PP}-\mathrm{P})] \tag{1}$$

where **M**, **R**, **V**, **P**, **W**, and μ are the nuclear masses, nuclear positions, nuclear velocities, density matrix, density matrix velocity, and fictitious mass for the electronic degrees of freedom, respectively. The first term in eq 1 is the kinetic energy of nuclei; the second term is the kinetic energy for the electronic degrees of freedom; the third term is the electronic energy of the system; and the fourth term is a constraints on the total number of electrons N_e and on the idempotency of the density matrix with a Largrangian multiplier matrix Λ. In the orthonormal basis, the Euler–Lagrange equations of motion of the nuclei and of the density matrix are[23]

$$\mathbf{M}\frac{d^2R}{dt^2} = -\left.\frac{\partial E(R,P)}{\partial R}\right|_P \tag{2}$$

and

$$\mu\frac{d^2P}{dt^2} = -\left[\left.\frac{\partial E(R,P)}{\partial P}\right|_R + \Lambda P + P\Lambda - \Lambda\right] \tag{3}$$

The nuclei and density matrix are propagated with eqs 2 and 3, respectively. In CPDM, the molecular orbitals rather than the density matrix are propagated[19]

$$\mu\frac{d^2\psi}{dt^2} = -\left.\frac{\partial E(R,\psi)}{\partial \psi}\right|_R + \text{constraints} \tag{4}$$

Proper choosing of the fictitious mass of the electronic degrees of freedom and time step in ADMP simulations ensures a good energy conservation and the adiabaticity between the nuclear and electronic motions.[23,24] One important advantage of ADMP over the traditional CPMD is that ADMP can treat the isotope effect of hydrogen and deuterium,[24,25] which becomes an important dynamical factor in processes involving hydrogen atoms, e.g. proton transfer and PH bond vibrations and rotations. In ADMP simulations, the initial velocities of nuclei are randomly generated to simulate Boltzmann distribution.[23−25] The kinetic energy of a system also affects the adiabaticity between nuclei and electrons; this kinetic energy should be much smaller than the gap between the highest occupied molecular orbital (HOMO) and the lowest unoccupied molecular orbital (LUMO) of the system to ensure that the dynamics is simulated close to the Born–Oppenheimer ground-state surface, well below the lowest excited electronic state.[24,25] Usually a thermostating method, such as Nosé-Hoover thermostats,[28] on the electronic subsystem is applied when the kinetic energy of the system is too high. MD simulation provides complementary information about the thermodynamic, dynamical properties, and microscopic motions of nuclei of a chemical reaction. However, due to the computing effort on the electronic energy of the system, ADMP is time-consuming for large systems, though the ONIOM model can be applied in some cases.[29] Furthermore, due to the nature of AIMD, the zero-point vibrational energy (ZPVE) correction is not incorporated for the PES.

Quantum chemical package Gaussian 03[30] has been employed for the calculations. Various stationary points (e.g. **cisTS**, **gammaTS**, **cis**, **TS1**, **TS2**, and **TS3**) on the PES from QM calculations[6] are used as starting points for MD simulations for the Staudinger reaction. To be consistent with previous QM calculations, B3LYP[31,32] with 6-31G(d) basis set is used for MD simulations. To get appropriate PES for the **TS3** region, the ZPVE correction is included in the static QM calculations.[6] However, no ZPVE corrections are considered in ADMP simulations in our present studies. The performance of B3LYP with the 6-31G(d) basis set[6,33] gives us confidence in applying this method in present MD simulations.

The coordinates of the system in the Staudinger reaction during ADMP simulations are extracted for single point QM calculations with natural bond orbital (NBO)[34] and molecular orbital analysis. In ADMP simulations, two different conditions are employed, adiabatic MD and thermostatic MD. In adiabatic MD, once the system is given an initial kinetic energy, the total energy is conserved during the entire simulation; most of the ADMP simulations are carried out under this condition. In thermostatic MD simulations, the kinetic energy of the system is kept constant. In all ADMP simulations, no ZPVE correction is made. For convenience, the initial kinetic energy for each ADMP simulation is chosen to be 0.01 eV (6.3 kcal/mol) for transition states or a multiple of 0.01 eV for minima. All of the kinetic energies are chosen to be much smaller than the HOMO–LUMO gap of all the stationary points investigated to keep the trajectories close to the ground-state PES and well below any excited-state PES. The smallest HOMO–LUMO gap is 3.08 eV (71.0 kcal/mol) for **transTS**, which is much larger than any of the initial kinetic energies added to the system at the stationary points. Last, due to the finite number of trajectories we have sampled, we do not claim that our results are statistically accurate; rather we are confident about the qualitative understanding derived from the ADMP simulations presented hereafter.

III. Results and Discussion

A. **gammaTS of $PH_3 + N_3H$**. Table 1 and Scheme 3 display the energies and reaction profiles of the Staudinger reaction, respectively. The ADMP simulations starting from **gammaTS** are performed with time step 0.2 fs for 400 fs; the system has 6.3 kcal/mol (0.01 eV, another value could also be chosen) initial kinetic energy with fictitious electronic mass of 0.1 amu Bohr^2. These ADMP simulations end with either the reactants ($PH_3 + N_3H$) or the products ($N_2 + H_3P{=}NH$) with **gammaTS** bridging in between.

B. **cisTS of $PH_3 + N_3H$.** With the same conditions, ADMP simulations are carried out for **cisTS** for 2 ps. The change of potential energy of the system during simulations and average polarizability of some selected points are shown in Figure 1. In the reverse reaction direction to reactants PH_3 and N_3H, **cisTS** completely dissociates to PH_3 and N_3H around 84 fs as shown in Figure 1; at this stage, the PN_α and PN_γ distances are 4.4 and 4.1 Å, respectively. After the dissociation, the potential energy of the system keeps constant with small fluctuations. The dissociation energy is 21 kcal/mol, i.e. the system needs 21 kcal/mol to initialize the Staudinger reaction; this is in good agreement with our recent DFT calculations if the ZPVE correction is not included.[15]

The average polarizability decreases along the reverse reaction trajectory; this indicates that solvent effects on the Staudinger reaction ($PH_3 + N_3H$) will get stronger as PH_3 approaches N_3H in the initial attack. The average polarizability of the system begins to increase at 40 fs, when the strong interaction between PH_3 and N_3H occurs. (This is further verified by charge transfer between these two reactants in Figure 11.)

Table 1. HOMO−LUMO Gaps (in eV) and the Relative Electronic Energies (with and without the ZPVE Correction) and the Relative Gibbs Free Energies (at 1 atm and 298 K) of the Stationary Points along the Staudinger Reaction[a]

	gammaTS	transTS	cisTS	trans	TS1	cis	TS2	int	TS3	products
HOMO−LUMO gap	4.24	3.08	5.07	5.35	4.90	5.80	5.56	5.54	5.67	
electronic (no ZPVE)	32.8	48.2	21.6	25.5	32.3	15.8	26.4	25.6	27.4	−30.1
electronic (with ZPVE)	33.4	50.3	23.9	29.3	36.0	19.9	29.4	29.0	28.8	−29.2
Gibbs	41.9	59.6	33.2	38.7	45.7	29.7	39.5	38.8	39.3	−28.8

[a] All relative energies are measured with respect to that of the reactants and in kcal/mol.

Scheme 3. Reaction Profiles of the Staudinger Reaction of PH_3 + N_3H[a]

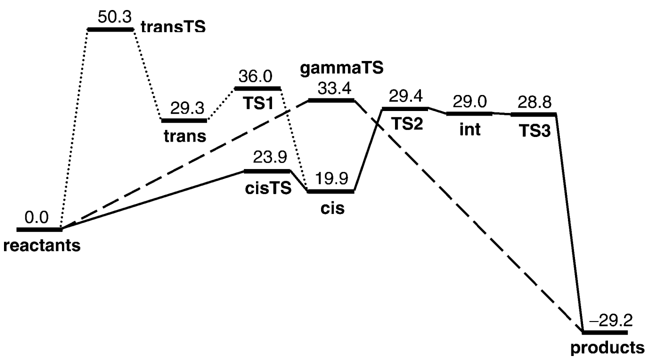

[a] The numbers are relative electronic energy with the ZPVE correction (in kcal/mol) of stationary points (measured with respect to that of the reactants).

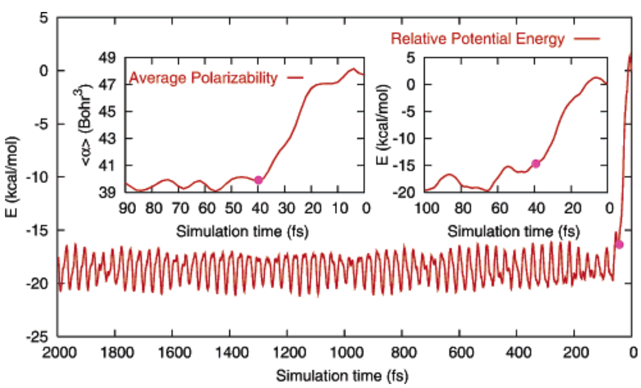

Figure 1. The relative potential energy (in kcal/mol) of the system to **cisTS** during ADMP simulation of 2 ps. The inserts are the average polarizability (in Bohr[3]) of system during the first 90 fs simulation and the relative potential energy for the first 100 fs, respectively.

The potential energy, geometric changes, and molecular orbital (MO) interactions between N_3H and PH_3 of some selected points for the first 100 fs simulations are shown in Figure 2. From the geometries of the five points shown in Figure 2, one notices that bond distance difference between $R_{PN\alpha}$ and $R_{PN\gamma}$ increases as PH_3 approaches N_3H. This means that the initial approach of PH_3 to N_3H for the cis attack is not directly toward N_α: P approaches rather simultaneously to N_α and N_γ. As getting close to N_3H, PH_3 moves attractively toward N_α in N_3H due to the electrostatic attraction and covalent interaction. It is very evident from the structure and molecular orbtials of the five points in Figure 2 that the motion of PH_3 approaching N_3H is translation concurrently with rotation of PH_3. Due to the relative orientation of PH_3 to N_3H, the molecular orbital overlap begins to turn on at 40 fs with $R_{PN\alpha}$ and $R_{PN\gamma}$ distances of 2.9 and 3.2 Å, respectively, as PH_3 approaches N_3H; the electrostatic attraction should play a prominent role for the initial approach of PH_3 to N_3H (more discussed later).

At point **E** in Figure 2, there is no covalent interaction (MO overlap) between PH_3 and N_3H, and the three MOs shown are the lone pair electrons of N and P. As the two molecules get closer at **D**, the MOs of the lone pair electrons on P and N adjust themselves according to the relative orientation of PH_3 and N_3H and no MO overlap occurs. When the two molecules get closer at point **C**, orbital overlap and charge transfer between PH_3 and N_3H occur as indicated by the relevant MOs. P donates electrons to N_γ from its lone pair, and N_α back-donates the lone pair to P through orbital overlap. This explains the strong interaction of P with both N_α and N_γ in **cisTS**. As these two molecules get closer as manifested by points **B** and **A**, the covalent interactions get stronger (more MOs for **A**, **B**, **C**, and **D** are shown in Figure 2s of the Supporting Information), which help to overcome the initial reaction barrier to reach intermediate, **cis**. The empty d orbitals on P have very limited contribution to the interaction of PH_3 with N_3H according to the NBO analysis.

In another ADMP simulation of **cisTS** with the same conditions (time step 0.2 fs and 6.3 kcal/mol initial kinetic energy) for 2 ps, PH_3 attacks N_α and forms PN_α bond after 12 fs, thus rendering the formation of the **cis** intermediate. The system, trapped in the **cis** potential well, fluctuates around the structure of **cis** after reaching **cis** during the 2 ps ADMP simulations.

The same conditions are applied to ADMP simulations of **cis**, with 6.3 kcal/mol of initial kinetic energy. Under this condition, the system is trapped in the **cis** potential well for 4 ps; this indicates that the system does not have enough energy in the reaction coordinates to overcome the reaction barriers to return to reactants or to tautomerize to **trans** or isomerizes to **int**. Increasing the initial kinetic energy to 25.2 kcal/mol (0.04 eV/mol) in an ADMP simulation of 2 ps starting from **cis** drives the system out of the **cis** potential well. The changes of potential energy of the system along the trajectory are shown in Figure 3. The system tries to open the $PN_\alpha N_\beta N_\gamma$ four-membered ring to reach a local maximum **A** at 54 fs (as shown in Figure 3) with $A_{PN\alpha N\beta}$ = 145°, $A_{N\alpha N\beta N\gamma}$ = 126°, and $R_{PN\gamma}$ = 3.4 Å and then returns to **cis** and moves out of the **cis** potential well to reach the structure at point **B** similar to **TS2** at 136 fs. The system then repeats the $PN_\alpha N_\beta N_\gamma$ ring-opening and ring-closing motions till 300 fs. There is a small potential energy plateau after 300 fs of ADMP simulation, where PH_3 rotates about the PN_α bond from 300 to 370 fs resembling **cis** → **TS2** motion (**D** → **E**). After 370 fs, the system returns to **cis** and internally rotates about the $N_\alpha N_\beta$ bond to reach 35° for the dihedral angle $D_{PN\alpha N\beta N\gamma}$ at point **F**. Along with this internal rotation, the system stretches PN_α, $N_\alpha N_\beta$, and N_β N_γ bonds

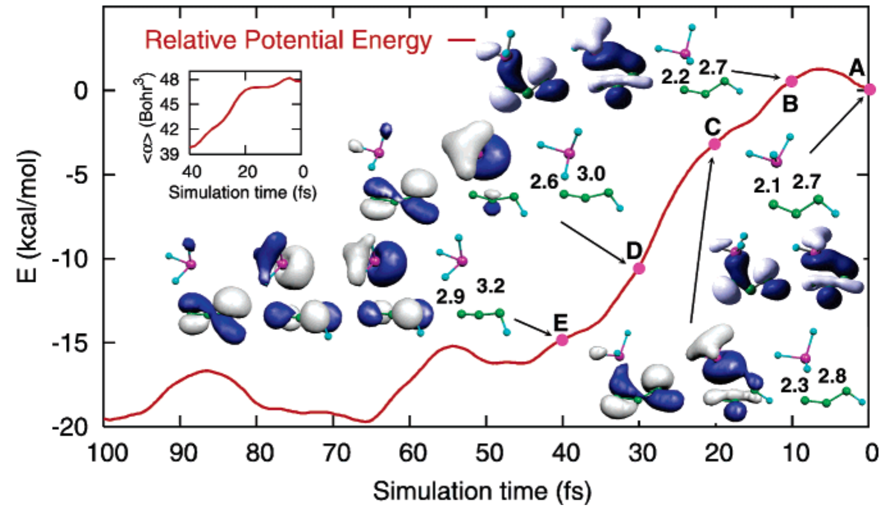

Figure 2. The relative potential energy (in kcal/mol) of the system to **cisTS** during the first 100 fs of a total 2 ps ADMP simulation with 0.2 fs time step and 6.3 kcal/mol initial kinetic energy. The pair of left and right numbers in the structures are the bond distances of P to N_α and N_γ, respectively. Simulation times for the selected points are **A** at 0 fs, **B** at 10 fs, **C** at 20 fs, **D** at 30 fs, and **E** at 40 fs. Only those molecular orbitals relevant to the interaction between PH_3 and N_3H are shown (from left to the right): HOMO-2, HOMO-1, and HOMO for point **E**, HOMO-2 and HOMO for points **D** and **C**, and HOMO-2 and HOMO-1 for points **B** and **A**. HOMO-n is the *n*th orbital below the HOMO. The molecular orbitals are drawn with isovalue 0.04 Å^{-3}. More molecular orbitals for points **A**, **B**, **C**, and **D** are shown in Figure 2s in the Supporting Information.

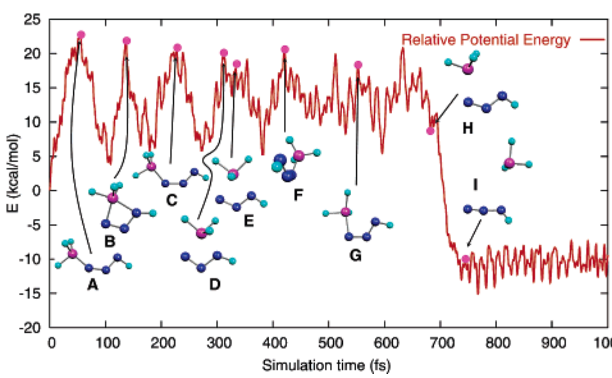

Figure 3. The relative potential energy (in kcal/mol) of the system to **cis** during the first 1 ps of a total 2 ps ADMP simulation, starting from **cis** with 0.2 fs time step and 25.2 kcal/mol initial kinetic energy. Simulation times for the selected points are **A** at 56 fs, **B** at 136 fs, **C** at 223 fs, **D** at 309 fs, **E** at 330 fs, **F** at 416 fs, **G** at 564 fs, **H** at 679 fs, and **I** at 743 fs.

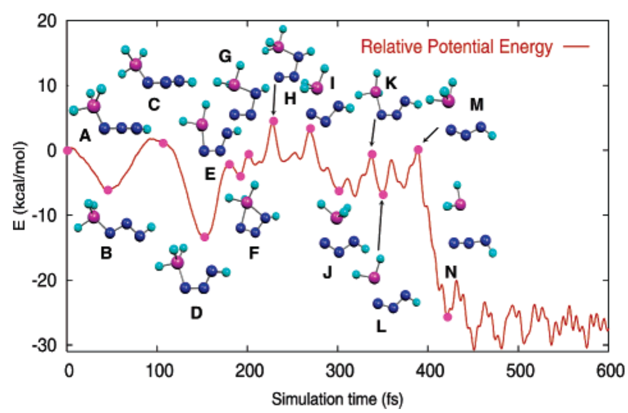

Figure 4. The relative potential energy (in kcal/mol) of the system to **TS1** during the first 600 fs of a total 2 ps ADMP simulation, starting from **TS1** with 0.2 fs time step and 6.3 kcal/mol initial kinetic energy. Simulation times for the selected points are **A** at 0 fs, **B** at 48 fs, **C** at 105 fs, **D** at 153 fs, **E** at 179 fs, **F** at 190 fs, **G** at 201 fs, **H** at 228 fs, **I** at 271 fs, **J** at 301 fs, **K** at 334 fs, **L** at 349 fs, **M** at 379 fs, and **N** at 421 fs.

from 410 to 600 fs to prepare for the right energy and momentum distributions for PH_3 and N_3H dissociation as represented by point **G**. After 640 fs, the system begins to dissociate back to PH_3 and N_3H, as indicated by the drastic drop of potential energy starting from point **H**. At 740 fs, the system completely dissociates to PH_3 and N_3H with $R_{PN\alpha} = 4.2$ Å and $R_{PN\gamma} = 3.3$ Å, as indicated by point **I**.

C. TS1 of PH_3 + N_3H. If the ADMP simulations start from **TS1** (**A**) (as shown in Figure 4), the system comes to **trans** (**B**) and then goes to **cis** (**D**) by overcoming **TS1** (**C**). The reaction barrier from **trans** to **cis** is 7.5 kcal/mol, and the reverse barrier is 11.9 kcal/mol from **cis** to **trans**, which are in good agreement with our previous QM calculations.[6] The deviation of these barriers from those of the QM studies is expected, since the MD simulation usually does not go through minimum energy path and does not include the ZPVE correction. By overcoming an 11.1 kcal/mol reaction barrier at **TS2** (**E**), the system reaches **int** (**F**) and then comes to a potential energy plateau involving the migration of PH_3 from N_α to N_γ and backward migration from N_γ to N_α as indicated by points **E**, **F**, **G**, **H**, **I**, **J**, and **K** till 380 fs. The most noticeable geometric change during the PH_3 migration is the rotation of PH_3, which is clearly manifested by the relative positions of the three H atoms on P of PH_3. This rotation is the driving force for the PH_3 migration, breaking the PN_α bond and forming the PN_γ bond. After 380 fs, the system uses 50 fs to dissociate back to PH_3 and N_3H. The tautomerization from **cis** to **trans** and isomerization from **cis** to **int** are competitive processes according to this ADMP simulation, and the isomerization from **cis** to **int** is favored energetically.

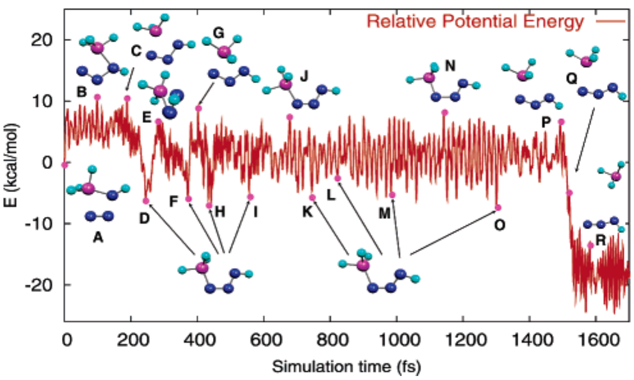

Figure 5. The relative potential energy (in kcal/mol) of the system to **TS3** during the first 1.6 ps of a total 2 ps ADMP simulation, starting from **TS3** with 0.2 fs time step and 12.6 kcal/mol initial kinetic energy. Simulation times for the selected points are **A** at 0 fs, **B** at 105 fs, **C** at 173 fs, **D** at 246 fs, **E** at 288 fs, **F** at 369 fs, **G** at 402 fs, **H** at 440 fs, **I** at 554 fs, **J** at 677 fs, **K** at 772 fs, **L** at 857 fs, **M** at 991 fs, **N** at 1140 fs, **O** at 1384 fs, **P** at 1510 fs, **Q** at 1532 fs, and **R** at 1590 fs.

D. **TS3 of $PH_3 + N_3H$**. Previous QM calculations[6−8] have all predicted that the PES around **TS3** is very flat: the energy of **TS3** after the ZPVE correction is even lower than that of **int**[6,7] (as shown in Scheme 3). The only conclusion could be drawn here is that the energies of **TS3** and **int** are very close, and essentially there is only one reaction barrier from **cis** to the final products.[6] Starting from **TS3** with 6.3 kcal/mol initial kinetic energy and 0.2 fs time step in adiabatic ADMP simulations, the system is trapped in the **cis** potential well after it goes through **int** and gets over **TS2** within 4 ps. More initial kinetic energy might help the system overcome the reaction barrier to dissociate back to PH_3 and N_3H. A trajectory of ADMP simulation starting from **TS3** with time step 0.2 fs and 12.6 kcal/mol initial kinetic energy is shown in Figure 5. Around 250 fs, the system reaches **cis** (point **D** in Figure 5) after going through **int** (similar to point **B**) and **TS2** (similar to point **C**). The PES of this region of **TS2**, **int**, and **TS3** is very flat, consistent with previous QM predictions.[6−8] At 288 fs, the system tries to tautomerize to **TS1** by twisting dihedral angle $D_{PN\alpha N\beta N\gamma}$ to around 30° (point **E** in Figure 5) and returns to **cis** at 369 fs and switches to $PN_\alpha N_\beta N_\gamma$ ring-opening and ring-closing motions. The ring-opening and ring-closing motions companied with bond stretching take 700 fs before preparing the system to dissociate back to PH_3 and N_3H. At about 1.51 ps, the system begins to dissociate to PH_3 and N_3H by redistributing internal energy and momentum from **cisTS** (point **P**). Once the system goes over **cisTS**, the potential energy of the system drops quickly along the dissociation path. Starting from **TS3** with 0.2 fs time step and 6.3 kcal/mol initial kinetic energy, the ADMP simulation toward the N_2 dissociation is straightforward, and the system dissociates to N_2 and $H_3P{=}NH$ quickly and smoothly as shown in Figure 6.

During the N_2 dissociation, the most visible motions within the system are the internal rotation of NH about the PN_γ bond and the departure of N_α and N_β from the system. Within the first 40 fs, the major motions of the system are N_2 formation and detachment, which is in the forward direction from **TS3**.[6] N_α and N_β are not leaving at the same speed:

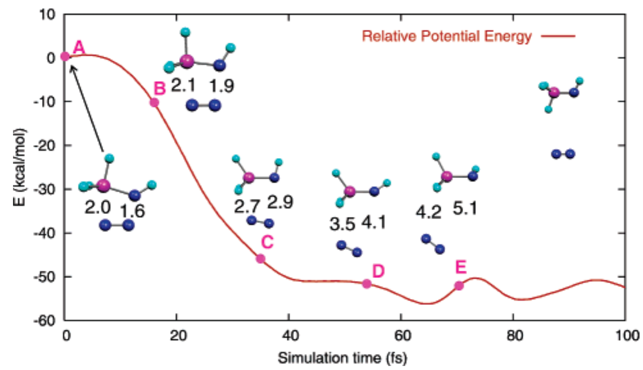

Figure 6. The relative potential energy (in kcal/mol) of the system to **TS3** during the first 100 fs of a total 400 fs ADMP simulation, starting from **TS3** with 0.2 fs time step and 6.3 kcal/mol initial kinetic energy. Simulation times for the selected points are **A** at 0 fs, **B** at 16 fs, **C** at 36 fs, **D** at 54 fs, and **E** at 70 fs. The upper-right structures are the final products, $H_3P{=}NH$ and N_2, drawn for comparison.

N_β leaves faster than N_α does (as indicated by points **B** and **C** in Figure 6). After 40 fs, N_2 dissociates from $H_3P{=}NH$, and a portion of the residual energy redistributes into the internal rotation of NH about the PN bond in $H_3P{=}NH$, which is clearly indicated by the relative positions of the hydrogen atoms on P and the hydrogen atom on N (points **D** and **E** in Figure 6). In **TS3**, the hydrogen atom on N_γ is in the eclipse position to one of the hydrogen atoms on P and is in the staggered conformation to the remaining atoms on P in $H_3P{=}NH$. The dissociation energy of the system to $H_3P{=}NH$ and N_2 from **TS3** is about 55 kcal/mol, which is consistent with our previous QM studies.[6]

The ADMP simulations with 0.2 fs time step and 6.3 kcal/mol initial kinetic energies (12.6 kcal/mol for **TS3**) started from **gammaTS**, **cisTS**, **TS1**, and **TS3** reproduce the potential energy surface as predicted in our previous QM studies[6] and reveal details about the dynamics on the PES. ADMP simulations starting from **TS2** end with dissociation back to PH_3 and N_3H.

E. **Thermostatic MD Simulations.** In chemical reactions, the adiabatic condition might not be maintained, and most reactions are thermostatic. The thermostatic MD simulations should be more appropriate to uncover the reaction mechanism in an actual chemical environment. The final step of the Staudinger reaction only takes place at room temperature, and a complex forms at lower temperature before the whole reaction completes.[35] To reproduce the experimental condition, an ADMP simulation with 0.2 fs time step at 298 K is carried out starting from **TS3** for 2 ps. Shown in Figure 7, the trajectory of the potential energy is different from the adiabatic trajectory with 12.6 kcal/mol initial kinetic energy (as shown in Figure 5). However, the qualitative evolutions of the system in the two trajectories are similar, both isomerize to **cis** first, then undergo $PN_\alpha N_\beta N_\gamma$ ring opening followed by PH_3 shift, and finally dissociate to PH_3 and N_3H (shown by structures of the system during the simulations in Figures 5 and 7). The system dissociates back to PH_3 and N_3H after 600 fs in the thermostatic ADMP simulation, which is much faster than that in the adiabatic ADMP simulation. Under the same condition, an ADMP simulation starting from

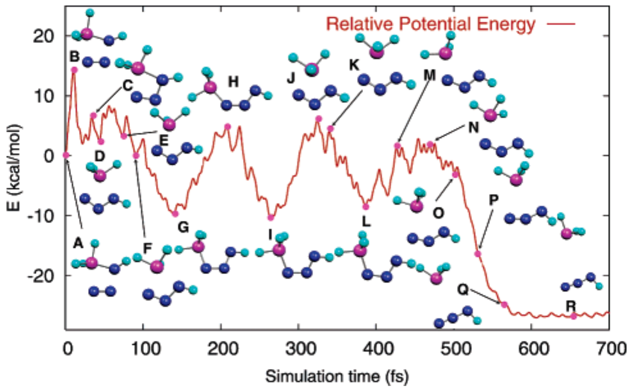

Figure 7. The reaction potential energy (in kcal/mol) of the system to **TS3** during the first 700 fs of a total 2 ps thermostatic ADMP simulation, starting from **TS3** at 298 K with 0.2 fs time step. Simulation times for the selected points are **A** at 0 fs, **B** at 11 fs, **C** at 32 fs, **D** at 43 fs, **E** at 72 fs, **F** at 88 fs, **G** at 138 fs, **H** at 207 fs, **I** at 267 fs, **J** at 323 fs, **K** at 341 fs, **L** at 385 fs, **M** at 427 fs, **N** at 467 fs, **O** at 506 fs, **P** at 530 fs, **Q** at 567 fs, and **R** at 643 fs.

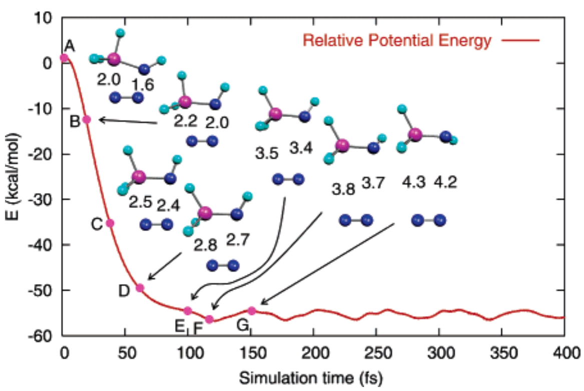

Figure 8. The relative potential energy (in kcal/mol) of the system to **TS3** during a total 400 fs thermostatic ADMP simulation, starting from **TS3** with 0.2 fs time step at 298 K. Simulation times for the selected points are **A** at 0 fs, **B** at 20 fs, **C** at 40 fs, **D** at 60 fs, **E** at 100 fs, **F** at 120 fs, and **G** at 150 fs. The pair of left and right numbers are PN_α and $N_\beta N_\gamma$ bond distances (in Å), respectively.

TS3 is carried out for 400 fs, and the system dissociates forward to $H_3P{=}NH$ and N_2 (as shown in Figure 8). Similar to the adiabatic dissociation (as shown in Figure 6), the system dissociates forward to $H_3P{=}NH$ and N_2, followed by the internal rotation of NH about the PN bond in $H_3P{=}NH$. In the thermostatic dissociation, N_α and N_β leave $H_3P{=}NH$ at the same speed. The thermostatic dissociation has a similar dissociation energy to that of the adiabatic dissociation (about 56 kcal/mol). From the above ADMP simulations, the complete reaction pathway of the Staudinger reaction is explored, and the ADMP simulations corroborate the previous QM predictions.[6−8]

To get more details on the evolution of the system during the Staudinger reaction, it is necessary to do structural analysis on the trajectory. The thermostatic ADMP simulation starting from **TS3** at 298 K is analyzed accordingly. $R_{PN\alpha}$ and $R_{PN\gamma}$ and the bond distance fluctuations of $R_{N\gamma H}$ and R_{PH} during the simulation are shown in Figure 9. The

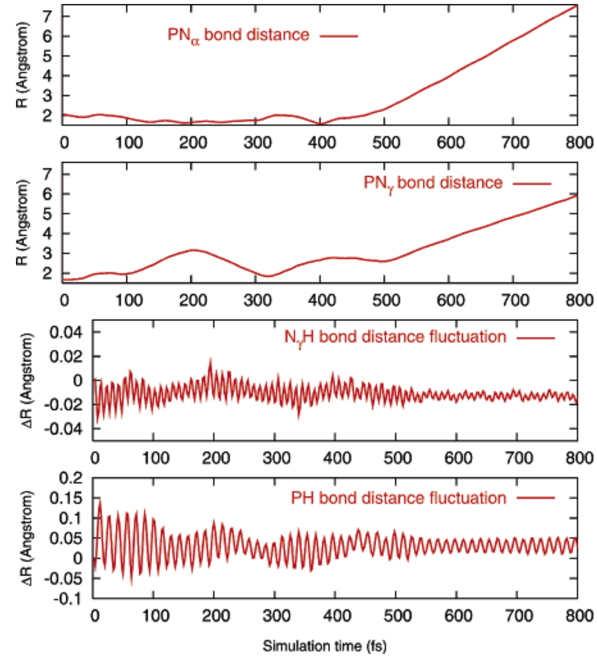

Figure 9. Bond distances $R_{PN\alpha}$ and $R_{PN\gamma}$ and bond distance changes of $R_{N\gamma H}$ and R_{PH} with respect to **TS3** during the first 800 fs of a total 2 ps thermostatic ADMP simulation, starting from **TS3** at 298 K. The hydrogen atom on P is at the same side of the hydrogen atom on N_γ in **TS3**.

hydrogen atom of R_{PH} on P is at the cis position to the hydrogen atom on N_γ, and all the structural data pertinent to hydrogen atom on P are based on this hydrogen atom. During the course of the reaction, bond distance $R_{PN\gamma}$ changes much more than $R_{PN\alpha}$ before dissociation back to PH_3 and N_3H. Initially, PH_3 approaches N_α and N_γ at the similar distance from far away—ca. 700 fs. From **TS3** to **cis**, bond distance $R_{N\gamma H}$ does not change much, while bond distance R_{PH} changes a lot (mainly stretching). It can be inferred that the PH bond stretching facilitates the PH_3 migration between N_α and N_γ. Figure 10 shows bond angle $A_{N\alpha N\beta N\gamma}$ and dihedral angles $D_{PN\alpha N\beta N\gamma}$, $D_{N\alpha N\beta N\gamma H}$, and $D_{HPN\alpha N\beta}$ of the trajectory. The value of $A_{N\alpha N\beta N\gamma}$ shows the linearity of the azide backbone during the simulation. When PH_3 and N_3H fall apart, $A_{N\alpha N\beta N\gamma}$ begins to increase: $A_{N\alpha N\beta N\gamma}$ reaches 175° at 470 fs from 120° at 475 fs. Dihedral angle $D_{PN\alpha N\beta N\gamma}$ indicates the planarity of the $PN_\alpha N_\beta N_\gamma$ four-membered ring and serves as a criterion for the system to tautomize from **cis** (close to 0°) to **trans** (close to 180°) through **TS1** (close to 90°). At 220 fs, the system tries to twist $D_{PN\alpha N\beta N\gamma}$ (point **H** in Figure 7) and returns to **cis** ca. 300 fs, which indicates that the system can tautomerize to **trans** from **cis** if provided with enough energy and proper energy and momentum distributions. The change of $D_{PN\alpha N\beta N\gamma}$ indicates that PH_3 does migrate from N_α to N_γ within the $N_\alpha N_\beta N_\gamma$ plane. Dihedral angle $D_{N\alpha N\beta N\gamma H}$ serves as an indicator for the involvement of H motion on N_γ in the Staudginer reaction: the change of this dihedral angle during the ADMP simulation indicates that the out-of-$N_\alpha N_\beta N_\gamma$H plane motion of H takes place all along the Staudinger reaction, especially during the PH_3 migration from N_α to N_γ as indicated by point **F** (at 88 fs) and point **J** (ca. 320 fs) in Figure 7. The rotation of PH_3 group during the reaction is indicated by dihedral angle $D_{HPN\alpha N\beta}$ shown

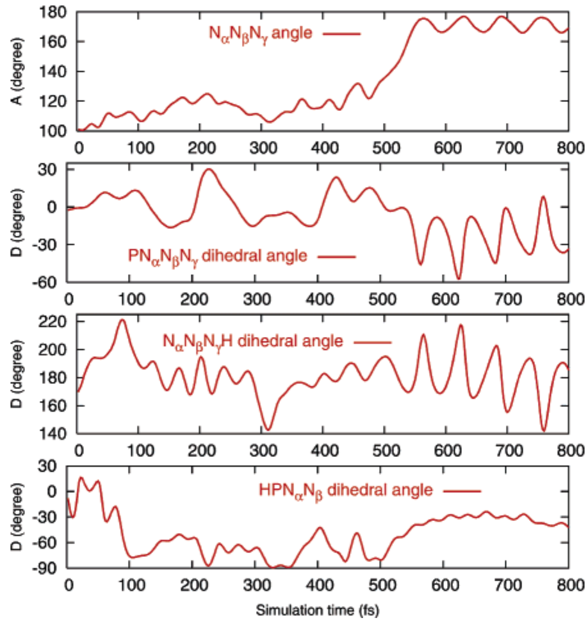

Figure 10. Bond angles $A_{N\alpha N\beta N\gamma}$ and dihedral angles $D_{PN\alpha N\beta N\gamma}$, $D_{N\alpha N\beta N\gamma H}$, and $D_{HPN\alpha N\beta}$ of the system with respect to **TS3** during the first 800 fs of a total 2 ps thermostatic ADMP simulation, starting from **TS3** at 298 K. The hydrogen atom on P is at the same side of the hydrogen atom on N_γ in **TS3**.

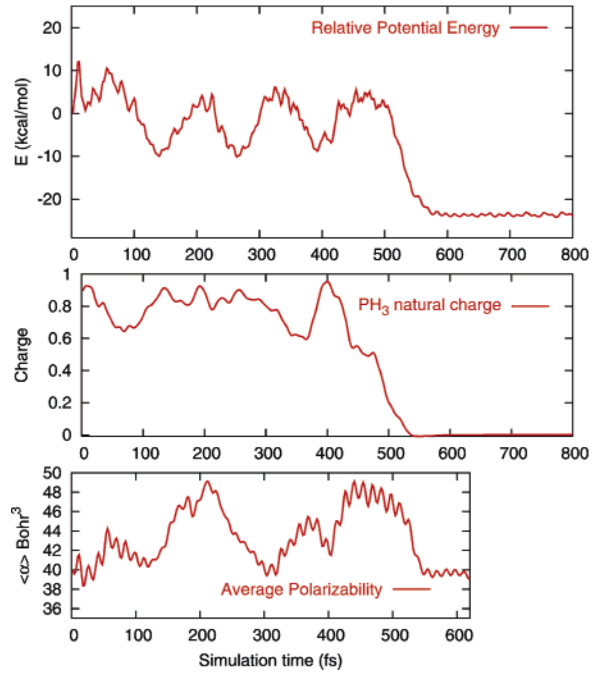

Figure 11. Relative potential energy and average polarizability of the system and natural charge of PH_3 unit of the system, based on single-point and thermostatic ADMP calculations at B3LYP with 6-31G(d) basis set, starting from **TS3** with 0.2 fs time step at 298 K. The total simulation time is 2 ps. Only the first 800 fs is shown for relative energy of the system and the natural charge of PH_3, and only the first 620 fs is shown for the averaged polarizability. The structures of the stationary points on the potential energy surface are displayed in Figure 7.

in Figure 10. The overall change of $D_{HPN\alpha N\beta}$ is more than 90° during the isomerization from **TS3** to **cis,** which clearly indicates that PH_3 rotation serves as a driving force for the PH_3 migration between N_α and N_γ. $D_{HPN\alpha N\beta}$ changes through the entire reaction pathway. The structural analysis indicates that (1) the PH_3 leaves (or approaches) N_α and N_γ with similar speeds when the system dissociates (or forms), (2) P is not always within the $N_\alpha N_\beta N_\gamma$ plane during the Staudinger reaction, and (3) the out-of-plane motion of the hydrogen atom on N_γ and the rotation of PH_3 facilitate the migration of PH_3 between N_α and N_γ. Bulky substituent groups hinder the rotation and increase the rotation barrier from **cis** to **TS3**. This is indeed the case for large substituent groups, as predicted by our previous QM studies.[6]

ADMP simulation is an approximation to BOMD on the PES and should be parallel to that of BOMD.[26,36] We performed single-point calculations with the ADMP trajectory starting from **TS3** at the same level of theory as before.[6] The relative energies of the single-point calculations to **TS3** are plotted in Figure 11. The relative energies of the single-point calculations are very similar to those of ADMP simulations, which verify the validity of the ADMP simulations. Figure 11 also shows the natural charge of PH_3 group during the ADMP simulation. The plot of the natural charge of PH_3 indicates the charge transfer between PH_3 and N_3H subunits during the Staudinger reaction. Around the dissociation, the charge transfer between PH_3 and N_3H decreases as the two groups fall apart, and the overall charge on each group diminishes around 540 fs when PN_α and PN_γ bond distances are about 3.0 Å. The natural charge on PH_3 group around the dissociation (or attacking) region along the trajectory indicates the electrostatic attraction plays an important role for the initial Staudinger reaction. During the Staudinger reaction, the average polarizability of the system (as shown in Figure 11) changes along with the reaction course, and the region around **TS3** has relatively small polarizability because of its compact structure. The polarizability increases as the system tries to twist $D_{PN\alpha N\beta N\gamma}$ to reach **TS1**. **cis** has small polarizability. As **cis** begins to dissociate back to PH_3 and N_3H, the polarizability increases as the system overcomes the **cisTS** barrier and decreases after overcoming the barrier. The change of polarizability of the system during the reaction course indicates that the solvent effect on the system varies with the reaction course: the polar solvent will stabilize all transition states and thus facilitates the overall reaction by decreasing the reaction barriers.

Some geometric data (bond distances $R_{PN\alpha}$, $R_{N\beta N\gamma}$, R_{PH}, and $R_{N\gamma H}$ and dihedral angles $D_{HPN\alpha N\beta}$, $D_{HPN\gamma H}$, and $D_{N\alpha N\beta N\gamma H}$) are plotted in Figures 12 and 13 for the dissociation trajectory to $H_3P{=}NH$ and N_2 starting from **TS3** in the thermostatic ADMP simulation. As shown in Figure 12, the N_α and N_β leave $H_3P{=}NH$ at the same speed. Dihedral angle $D_{HPN\gamma H}$ changes 30° at the first 90 fs, indicating that the leaving of N_α and N_β is the major motion during the N_2 dissociation. Dihedral angle $D_{HPN\gamma H}$ changes from −15° to −100° after the dissociation of N_2 during the first 90 fs, which is responsible for the potential energy fluctuation of the system after N_2 dissociation. Figure 13 displays bond distances R_{PH}, $R_{N\gamma H}$, and $R_{PN\gamma}$ along the dissociation. $R_{PN\gamma}$ decreases to the equilibrium P=N bond distance (around 1.56 Å) in $H_3P{=}NH$ after 50 fs. PN_γ bond stretches with the internal rotation

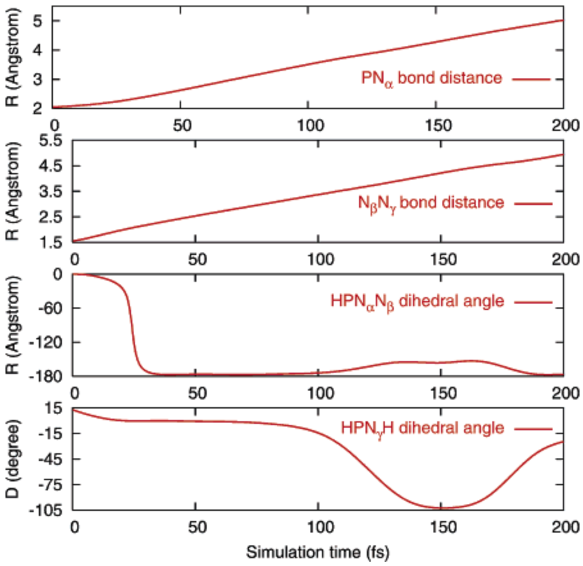

Figure 12. Bond distances $R_{PN\alpha}$ and $R_{PN\gamma}$ and dihedral angles $D_{HPN\alpha N\beta}$ and $D_{HPN\gamma H}$ with respect to **TS3** during the first 200 fs of a total 400 fs thermostatic ADMP simulation, starting from **TS3** at 298 K. The hydrogen atom on P is at the same side of the hydrogen atom on N_γ in **TS3**.

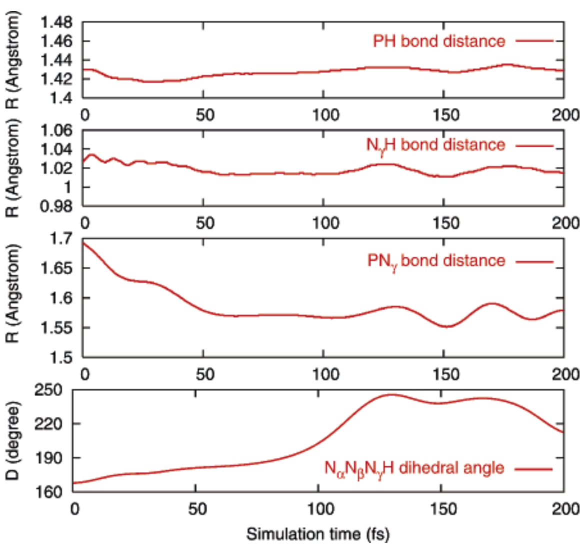

Figure 13. Bond distances R_{PH}, $R_{PN\gamma}$, and $R_{N\gamma H}$ and dihedral angle $D_{N\alpha N\beta N\gamma H}$ of the system with respect to **TS3** during the first 200 fs of a total 400 fs thermostatic ADMP simulation, starting from **TS3** at 298 K. The hydrogen atom on P is at the same side of the hydrogen atom on N_γ in **TS3**.

of $H_3P{=}NH$. From the changes of $D_{HPN\alpha N\beta}$, $D_{HPN\gamma H}$, and $D_{N\alpha N\beta N\gamma H}$, one can infer that it is $N_\gamma H$ that rotates about the PN bond in $H_3P{=}NH$ after the N_2 dissociation.

IV. Conclusions

In the present work, the Staudinger reaction of $PH_3 + N_3H$ has been simulated by ADMP molecular dynamics within DFT. The ADMP simulations starting from **cisTS**, **gamma-TS**, **cis**, **TS1**, **TS2**, and **TS3** reproduce the reaction pathways predicted by previous QM methods.[6−8] The details of the Staudinger reaction have been uncovered through the trajectories of the ADMP simulations:

(1) For the initial attack of PH_3 to N_3H, the P atom approaches N_α and N_γ with similar distances before significant interaction occurs between the two reactants. When PH_3 approaches N_3H ca. 3.0 Å, charge transfer from PH_3 to N_3H occurs, and the average polarizability of the system increases. This manifests that the strong electrostatic interaction occurs at this beginning stage and is the main driving force for the initial attack. The P atom interacts with both N_α and N_β when PH_3 approaches N_3H, as manifested by the molecular orbitals of the system during the initial reaction. The empty d orbitals of P play very limited role in this reaction.

(2) The Staudinger reaction goes through **cis**, **TS2**, **int**, and **TS3** to form phosphazene as predicted quantum mechanically before.[6−8] According to the ADMP simulations, **cis** can tautomerize to **trans** through **TS1** with proper conditions. The rotation of PH_3 and the stretching of PH bonds serve as dominant driving forces for the second phase of the Staudinger reaction from **cis** to **TS3**, according to the dihedral angle $D_{HPN\alpha N\beta}$ and the bond distance R_{PH} changes during the Staudinger reaction. Small substituent groups on P of phosphane, with faster PR_3 rotation and stronger PR stretching, will certainly facilitate the last stage (from **cis** to **TS3**) of the Staudinger reaction.

(3) The fact that the polarizability changes during the course of the reaction implies that different solvent effects are expected at different stages of the reaction. Appropriate solvent can alter the reaction course (e.g. tautormerization to **trans** from **cis**). Although the solvent effects are not taken into account in the present work explicitly, this omission should not qualitatively change the conclusion drawn here: polar solvent can facilitate the overall reaction by stabilizing all transition states and hence decreasing the reaction barriers. This understanding is based on the close correlation between the changes of the average polarizability and the potential energy of the system during the reaction. In our previous static quantum mechanical studies,[6] we compared the Staudinger reactions with different substituent groups on phosphane and azide in gas phase and in dimethyl sulfoxide and reached the same conclusion about the solvent effects for this reaction.

In summary, the Saudinger reaction of $PH_3 + N_3H$ has been studied with ab initio molecular dynamics. Our work demonstrates that the combination of quantum mechanical studies with ab initio molecular dynamics will enhance the strengths of both approaches and yield detailed mechanical and dynamical understanding of chemical reactions.

Acknowledgment. The financial support from the Natural Sciences and Engineering Research Council (NSERC) of Canada is gratefully acknowledged. We thank Professor Srinivasan S. Iyengar for a reprint of ref 26. W.Q.T. is grateful to Professor Yuriko Aoki at Kyushu University for her hospitality.

Supporting Information Available: Relevant molecular orbital diagrams of points **A**, **B**, **C**, and **D** in Figure 2 during an ADMP simulation starting from **cisTS** (Figure 2s). This material is available free of charge via the Internet at http://pubs.acs.org.

References

(1) Staudinger, H.; Meyer, J. *Helv. Chim. Acta* **1919**, *2*, 635.

(2) (a) Cordridge, D. E. C. *Phosphorus 2000: Chemistry, Biochemistry & Technology*; Elsevier: Amsterdam, 2000. (b) Irving, J. T. *Calcium and phosphorus metabolism*; Academic Press: New York, 1973.

(3) (a) Gololobov, Yu. G.; Zhmurova, I. N.; Kasukhin, L. F. *Tetrahedron* **1981**, *37*, 437. (b) Gololobov, Yu. G.; Zhmurova, I. N.; Kasukhin, L. F. *Tetrahedron* **1992**, *48*, 1353.

(4) Kato, H.; Ohmori K.; Suzuki, K. *Synlett* **2001**, *SI*, 1003.

(5) (a) Saxon, E.; Luchansky, S. J.; Hang, H. C.; Yu, C.; Lee, S. C.; Bertozzi, C. R. *J. Am. Chem. Soc.* **2002**, 124, 14893. (b) Saxon, E.; Bertozzi, C. R. *Science* **2000**, *287*, 2007. (c) Kato, H.; Ohmori K.; Suzuki, K. *Synlett* **2001**, *SI*, 1003.

(6) Tian, W. Q.; Wang, Y. A. *J. Org. Chem.* **2004**, *69*, 4299.

(7) Widauer, C.; Grützmacher, H.; Shevchenko I.; Gramlich, V. *Eur. J. Inorg. Chem.* **1999**, 1659.

(8) Alajarin, M.; Conesa, C.; Rzepa, H. S. *J. Chem. Soc., Perkin Trans.* **1999**, *2*, 1811.

(9) Goerlich, R.; Farkens, M.; Fischer, A.; Jones, P. G.; Schmutzler, R. *Z. Anorg. Allg. Chem.* **1994**, *620*, 707.

(10) Molina, P.; López-Leonardo, C.; Llamas-Botía, J.; Foces-Foces, C.; Fernández-Castaño, C. *Tetrahedron* **1996**, *52*, 9629.

(11) Alajarín, M.; Molina, P.; López-Leonardo, C. *Angew. Chem., Int. Ed. Engl.* **1997**, *36*, 67.

(12) Allen, L. C. *Int. J. Quantum Chem.* **1994**, *49*, 253.

(13) (a) Fukui, K. *Acc. Chem. Res.* **1981**, *14*, 363. (b) Gonzalez, C.; Schlegel, H. B. *J. Chem. Phys.* **1989**, *90*, 2154. (c) Gonzalez, C.; Schlegel, H. B. *J. Phys. Chem.* **1990**, *94*, 5523.

(14) Cornell, W. D.; Cieplak, P.; Bayly, C. I.; Gould, I. R.; Merz, K. M., Jr.; Ferguson, D. M.; Spellmeyer, D. C.; Fox, T.; Caldwell, J. W.; Kollman, P. A. *J. Am. Chem. Soc.* **1995**, *117*, 5179.

(15) Mackerell, A. D.; Bashford, D.; Bellott, M.; Dunbrack, R. L.; Evanseck, J. D.; Field, M. J.; Gao, J.; Guo, H.; Ha, S.; Joseph-McCarthy, D.; Kuchnir, L.; Kuczera, K.; Lau, T. F. K.; Mattos, C.; Michnick, S.; Nago, T.; Nguyen, D. T.; Prodhom, B.; Reiher, W. E.; Roux, B.; Schlenkrich, M.; Smith, J. C.; Stote, R.; Straub, J.; Watanabe, M.; Wiórkievicz-Kuczera, J.; Yin, D.; Karplus, M. *J. Phys. Chem. B* **1998**, *102*, 3586.

(16) Rappé, A. K.; Casewit, C. J.; Colwell, K. S.; Goddard, W. A. III; Skiff, W. M. *J. Am. Chem. Soc.* **1992**, *114*, 10046.

(17) *Modern methods for multidimensional dynamics computation in chemistry*; Thompson, D. L., Ed.; World Scientific: Singapore, 1998.

(18) Car, R.; Parrinello, M. *Phys. Rev. Lett.* **1985**, *55*, 2471.

(19) Marx, D.; Hutter, J. In *Modern methods and algorithms of quantum chemistry*; Grotendorst, J., Ed.; John von Neumann Institute for Computing: Jülich, 2000; Vol. 1, p 301.

(20) Hartke, B.; Carter, E. A. *J. Chem. Phys.* **1992**, *97*, 6569.

(21) Lippert, G.; Hutter, J.; Parrinello, M. *Theor. Chem. Acc.* **1999**, *103*, 124.

(22) Lippert, G.; Hutter, J.; Parrinello, M. *Mol. Phys.* **1997**, *92*, 477.

(23) Schlegel, H. B.; Millam, J. M.; Iyengar, S. S.; Voth, G. A.; Daniels, A. D.; Scuseria, G. E.; Frisch, M. J. *J. Chem. Phys.* **2001**, *114*, 9758.

(24) Iyengar, S. S.; Schlegel, H. B.; Millam, J. M.; Voth, G. A.; Scuseria, G. E.; Frisch, M. J. *J. Chem. Phys.* **2001**, *115*, 10291.

(25) Schlegel, H. B.; Iyengar, S. S.; Li, X.; Millam, J. M.; Voth, G. A.; Scuseria, G. E.; Frisch, M. J. *J. Chem. Phys.* **2002**, *117*, 8694.

(26) Iyengar, S. S.; Schlegel, H. B.; Voth, G. A.; Millam, J. M.; Scuseria, G. E.; Frisch, M. J. *Isr. J. Chem.* **2002**, *42*, 191.

(27) Gibson, D. A.; Ionova, I. V.; Carter, E. A. *Chem. Phys. Lett.* **1995**, *240*, 261.

(28) (a) Tuckerman, M. E. *J. Phys.: Condens. Matter* **2002**, *12*, R1297. (b) Nosé, S. *J. Chem. Phys.* **1984**, *81*, 511. (c) Hoover, W. G. *Phys. Rev. A* **1985**, *31*, 1695. (d) Martyna, G. J.; Klein, M. L.; Tuckerman, M. E. *J. Chem. Phys.* **1992**, *97*, 2635. (e) Tuckerman, M. E.; Parrinello, M. *J. Chem. Phys.* **1994**, *101*, 1302.

(29) Rega, N.; Iyengar, S. S.; Voth, G. A.; Schlegel, H. B.; Vreven, T.; Frisch, M. J. *J. Phys. Chem. B* **2004**, *108*, 4210.

(30) Gaussian 03, Revision B.05, Frisch, M. J.; Trucks, G. W.; Schlegel, H. B.; Scuseria, G. E.; Robb, M. A.; Cheeseman, J. R.; Montgomery, J. A., Jr.; Vreven, T.; Kudin, K. N.; Burant, J. C.; Millam, J. M.; Iyengar, S. S.; Tomasi, J.; Barone, V.; Cossi; Scalmani, G.; Rega, N.; Petersson, G. A.; Nakatsuji, H.; Hada, M.; Ehara, M.; Toyota, K.; Fukuda, R.; Hasegawa, J.; Ishida, M.; Nakajima, T.; Honda, Y.; Kitao, O.; Nakai, H.; Klene, M.; Li, X.; Knox, J. E.; Hratchian, H. P.; Cross, J. B.; Adamo, C.; Jaramillo, J.; Gomperts, R.; Stratmann, R. E.; Yazyev, O.; Austin, A. J.; Cammi, R.; Pomelli, C.; Ochterski, J. W.; Ayala, P. Y.; Morokuma, K.; Voth, G. A.; Salvador, P.; Dannenberg, J. J.; Zakrzewski, V. G.; Dapprich, S.; Daniels, A. D.; Strain, M. C.; Farkas, O.; Malick, D. K.; Rabuck, A. D.; Raghavachari, K.; Foresman, J. B.; Ortiz, J. V.; Cui, Q.; Baboul, A. G.; Clifford, S.; Cioslowski, J.; Stefanov, B. B.; Liu, G.; Liashenko, A.; Piskorz, P.; Komaromi, I.; Martin, R. L.; Fox, D. J.; Keith, T.; Al-Laham, M. A.; Peng, C. Y.; Nanayakkara, A.; Challacombe, M.; Gill, P. M. W.; Johnson, B.; Chen, W.; Wong, M. W.; Gonzalez, C.; Pople, J. A. Gaussian, Inc., Pittsburgh, PA, 2003.

(31) Becke, A. D. *J. Chem. Phys.* **1993**, *98*, 5648.

(32) (a) Lee, C.; Yang, W.; Parr, R. G. *Phys. Rev. B* **1988**, *37*, 785. (b) Miehlich, B.; Savin, A.; Stoll, H.; Preuss, H. *Chem. Phys. Lett.* **1989**, 157, 200.

(33) (a) Sheng, Y.; Musaev, D. G.; Reddy, K. S.; McDonald, F. E.; Morokuma, K. *J. Am. Chem. Soc.* **2002**, *124*, 4149. (b) Vereecken, L.; Peeters, J.; Bettinger, H. F.; Kaiser, R. I.; Schleyer, P. v. R.; Schaefer, H. F., III *J. Am. Chem. Soc.* **2002**, 124, 2781. (c) Jiao, H.; Frapper, G.; Halet, J.-F.; Saillard, J.-Y. *J. Phys. Chem. A* **2001**, *105*, 5945. (d) Beno, B. R.; Wilsey, S.; Houk, K. N. *J. Am. Chem. Soc.* **1999**, *121*, 4816. (e) Batra, R.; Giese, B.; Spichty, M.; Gescheidt, G.; Houk, K. N. *J. Phys. Chem.* **1996**, *100*, 18371. (f) Jursic, B.; Zdravkovski, Z. *J. Chem. Soc., Perkin Trans. 2* **1995**, 1223.

(34) Reed, A. E.; Curtiss, L. A.; Weinhold, F. *Chem. Rev.* **1988**, *88*, 899.

(35) Leffler, J. E.; Temple, R. D. *J. Am. Chem. Soc.* **1967**, *89*, 5235.

(36) The single-point calculations based on the ADMP trajectory are certainly different from the BOMD simulations, since the BOMD calculates the force from the converged charge density and potential.

CT049918X